Supplementary Information for "Experimental observation of topological large-area pseudospin-momentum locking waveguide states with exceptional robustness"

Liu He[1] Zhihao Lan[2*] Bin Yang[3] Jianquan Yao[1] Qun Ren[4, 5] Jian Wei You[5] Wei E. I. Sha[6] Yuting Yang[3*] Liang Wu[1*]

[1]Key Laboratory of Opto-Electronics Information Technology (Tianjin University), Ministry of Education, School of Precision Instruments and Opto-Electronics Engineering, Tianjin University, Tianjin, 300072, China

[2]Department of Electronic and Electrical Engineering, University College London, Torrington Place, London WC1E 7JE, United Kingdom

[3]School of Materials Science and Physics, China University of Mining and Technology, Xuzhou 221116, China

[4]School of Electrical and Information Engineering, Tianjin University, Tianjin 300072, China

[5]State Key Laboratory of Millimeter Waves, School of Information Science and Engineering, Southeast University, Nanjing, 210096, China

[6]Key Laboratory of Micro-Nano Electronic Devices and Smart Systems of Zhejiang Province, College of Information Science and Electronic Engineering, Zhejiang University, Hangzhou, 310027, China

*Corresponding authors (Zhihao Lan, email: lanzhihao7@gmail.com; Yuting Yang, email: yangyt@cumt.edu.cn; Liang Wu, email: wuliang@tju.edu.cn)

Supplementary Note 1: Tight-binding description of the photonic crystals

The photonic crystals considered in the main text could be described by a tight-binding (TB) Hamiltonian defined on the honeycomb lattice, and we consider the hexagonal unit cell that contains six lattice sites,

$$H_0 = -t_0 \sum_{<i,j>} \hat{c}_i^{\dagger} \hat{c}_j - t_1 \sum_{<i',j'>} \hat{c}_{i'}^{\dagger} \hat{c}_{j'}$$

where $t_0, t_1 > 0$ represent the nearest-neighbor (NN) hopping strengths within and between the hexagonal unit cells [1-3]. Moreover, to account for the change of R_2, one can introduce the next-next-nearest (NNN) hopping term[4]

$$H' = -t_2 \sum_{<<<i,j>>>} \hat{c}_i^{\dagger} \hat{c}_j$$

Where t_2 represent the next-next-nearest (NNN) hopping strengths within the hexagonal unit cells.

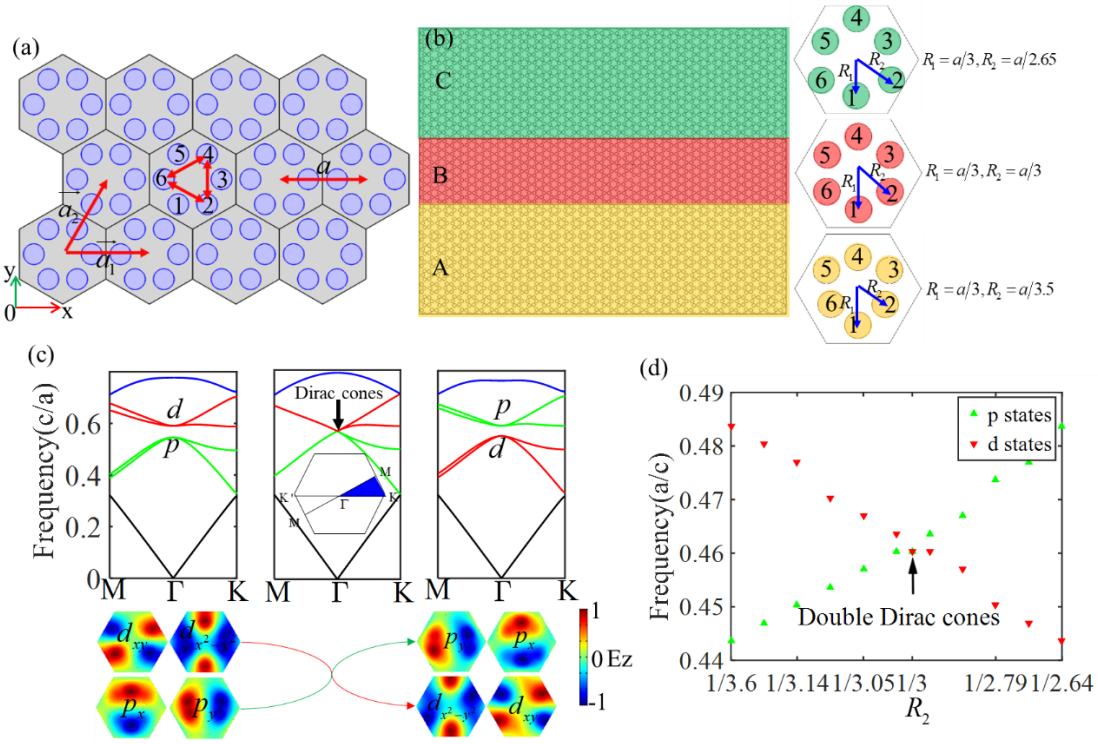

Figure S1 | Schematic of photonic crystals in graphene-like lattice and photonic band structures. a Schematic of photonic crystals in graphene-like lattice, where $\vec{a}_1$ and $\vec{a}_2$ denote the lattice vectors with a the lattice constant. Red arrows among sites 2, 4, and 6 denote the next-next-nearest (NNN) hopping within the hexagonal unit cell. **b** Schematic of $A|B_5|C$ heterostructure. The domains A, B and C are composed of different unit cells ($R_1 = a/3, R_2 = a/3.5$; $R_1 = a/3, R_2 = a/3$; $R_1 = a/3, R_2 = a/2.65$) respectively. **c** The photonic band structures for PhCs of the three domains shown in **b**. The bottom panel denotes the mode profiles at Γ for p (d) and d (p) states of trivial (nontrivial) PhCs. **d** Evolution of the band gap as a function of R_2 . The green and red dotted lines represent p and d states, respectively.

Supplementary Note 2: Projected band structures along the wavevector k_x for $A|B_x|C$

Figure S2 shows the projected band structures of the heterostructure $A|B_x|C$ as a function of x from $x = 0$ (without the middle domain B) to $x = 11$. Note that the dispersion curves of the topological waveguide modes (red lines) gradually evolve into an "X" shape as x increases, whereas non-topological waveguide modes (blue lines) gradually move from the bulk states (black regions) into the band gap but in general are gapped (see Figure S2b-g). As a result, operational bandwidth of the topological waveguide modes gradually decreases. This is because the coupling of the interface modes at A|B and B|C domain-walls become weaker as x increases, and as such more and more non-topological waveguide modes populate within the band gap. From Fig.S2, we can see that when x is small the coupling of the interface modes at A|B and B|C domain-walls is strong, resulting in a wide gap marked by the light orange region and when x is large, the coupling becomes weaker, i.e., the orange band gap becomes smaller, and more non-topological waveguide modes (blue lines) from the bulk states gradually move into the bulk gap marked by two dashed lines.

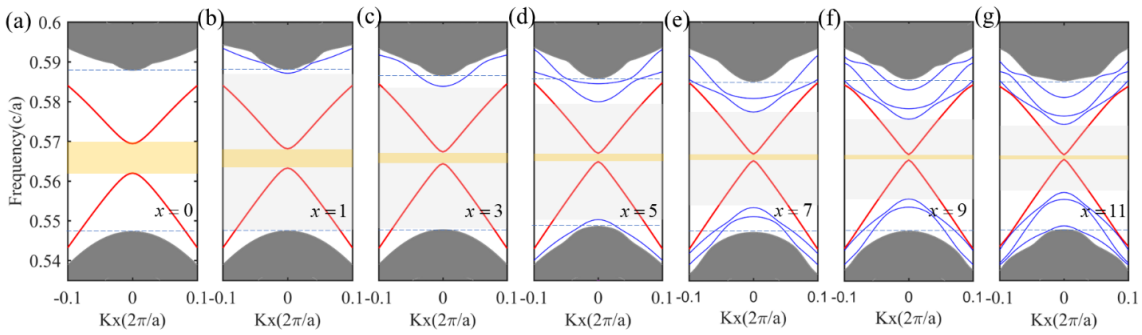

Figure S2 | Projected band structures of $A|B_x|C$ for x =0, 1, 3, 5, 7, 9 and 11. a-g Projected band structures, where black regions denote bulk states and red lines denote the topological large-area helical waveguide modes, whereas blue lines denote non-topological waveguide modes moving from bulk states into the band gap.

Supplementary Note3: Topological and non-topological waveguide modes in $A|B_5|C$

The heterostructure can support both topological and non-topological waveguide modes (see the blue and red dotted lines in Fig.S3a), however, their topological properties are very different, even though their field profiles show similar feature, i.e., their fields are distributed uniformly in the middle domain B and decay exponentially into domains A and C (see right panels of Fig. S3a, for the cases of non-topological modes). To demonstrate that the blue waveguide modes do not have topological properties, we excite these waveguide states using different polarized chiral sources, and the results in Figs. S3b-e show that they propagate in both directions no matter with straight or Z-shaped waveguide channel, indicating the lack of topological property with pseudospin-momentum-locking unidirectional propagations. In contrast, for the red waveguide states, the results in Figs.S3f-g show that they can be excited (by a chiral source) and propagate unidirectionally in the Z-shaped waveguide channel even with sharp bends, indicating the existence of topological property of these modes, such as pseudospin-momentum-locking unidirectional propagations and robustness against sharp bends.

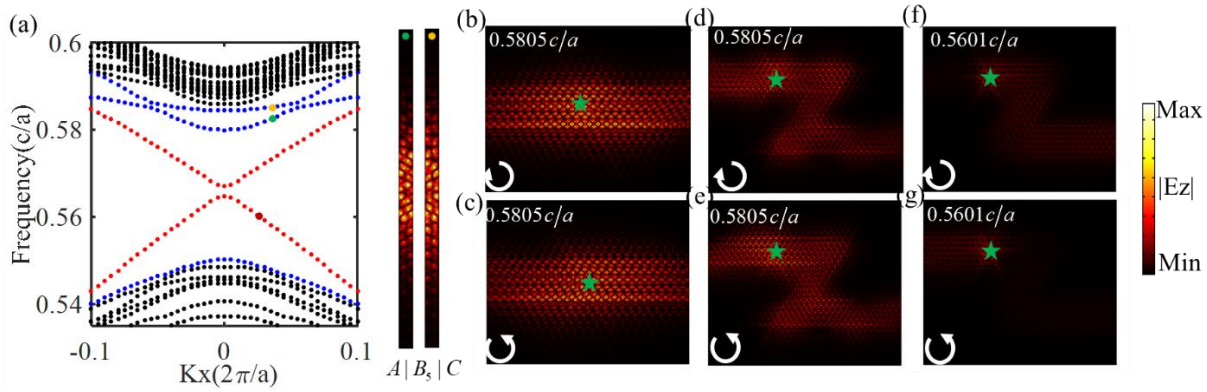

Figure S3 | Projected band structure of $A|B_5|C$ **and its waveguide modes. a** Projected band structure of $A|B_5|C$ (left), whereas right two panels show the modes profiles ($|E_z|$) of the non-topological waveguide modes at different eigenfrequencies marked by the green and yellow dots. **b-e** Excited non-topological waveguide states in $A|B_5|C$ with straight and Z-shaped waveguide channels for different polarized chiral sources. **f, g** Excited topological waveguide modes in $A|B_5|C$ with Z-shaped waveguide channel for different polarized chiral sources.

Supplementary Note 4: No topological waveguide modes in $A|B_5|A$

It is crucial that the outer two domains A and C have different topological properties in order for the heterostructure to support large-area pseudospin-momentum locking topological waveguide modes. To demonstrate this, we further study the projected band diagram of $A|B_5|A$, in which the two domains at each side of the middle domain B are the same and thus have the same topological property, i.e., the difference of their topological invariants across the middle domain is trivial. The projected band diagram of $A|B_5|A$ is shown in Fig. S4a, from which one can clearly see that the helical waveguide states are absent, and only gapped conventional waveguide states exist within the band gap. From the excited wave propagations shown in Figs.S4b-c, one can see that these are indeed waveguide modes but without the topological property of pseudospin-momentum locking unidirectional propagation.

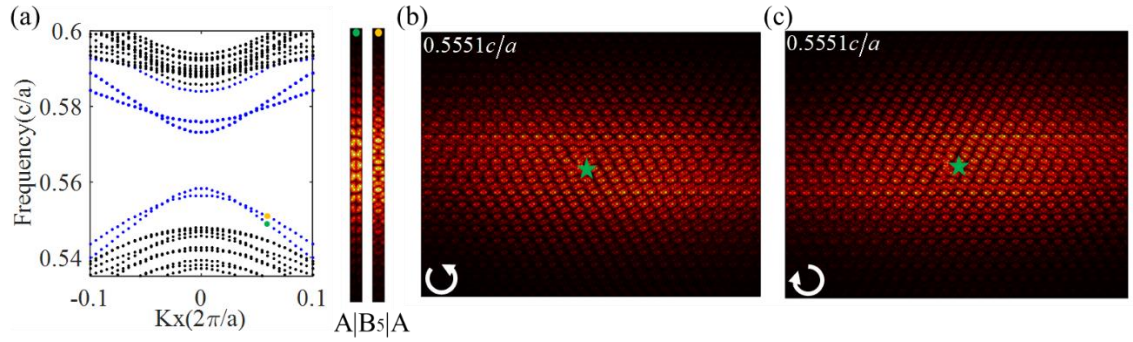

Figure S4 | Projected band structure of $A|B_5|A$ **and its waveguide states. a** Projected band structure of $A|B_5|A$ (left), whereas right two panels denote mode profiles ($|E_z|$) of the non-topological waveguide modes at different eigenfrequencies marked by the green and yellow dots. **b,c** Excited non-topological waveguide states in a straight waveguide channel for different polarized chiral sources.

Supplementary Note 5: Waveguide modes in $C|B_5|C$

Similar results as $A|B_5|A$ are also obtained in $C|B_5|C$, see Fig.S5.

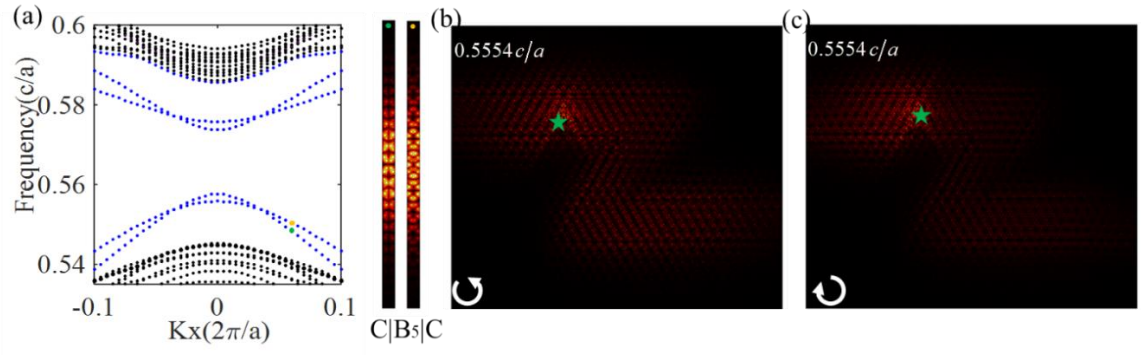

Figure S5 | Projected band structure of $C|B_5|C$ and its waveguide states. a Projected band structure of $C|B_5|C$ (left), whereas right two panels denote mode profiles ($|E_z|$) of the non-topological waveguide modes at different eigenfrequencies marked by the green and yellow dots. **b, c** Excited non-topological waveguide states in a Z-shaped waveguide channel for different polarized chiral sources.

Supplementary Note 6: Non-topological waveguide modes in $A|air|C$

To demonstrate that the middle domain B with gapless Dirac cone dispersion is also important for the heterostructure to support large-area pseudospin-momentum locking topological waveguide modes, we study the projected band diagram of $A|air|C$, where the middle domain B is replaced by air. From the result shown in Fig.S6a, one can see that there is a pair of waveguides modes within the bandgap, which however is different from those of ($A|B_x|C$, $C|B_5|C$, $A|B_5|A$). Note that the field profiles of these modes are also distributed mainly within the air and decay exponentially into domains A and C by checking the waveguide modes labelled as green and yellow dots. However, from the excited wave propagations shown in Figs.S6b-c, one can see that these are conventional waveguide states without any topological properties. These results demonstrate that the large-area pseudospin-momentum locking topological waveguide modes originate from the interplay of domains A and C with pseudospin band inversion and domain B with gapless double Dirac-cone dispersion. In contrast to air, the presence of a gapless Dirac cone dispersion in the middle domain is crucial, which allows the strong coupling and hybridization of the two topological interface modes associated with A|B and B|C domain-walls.

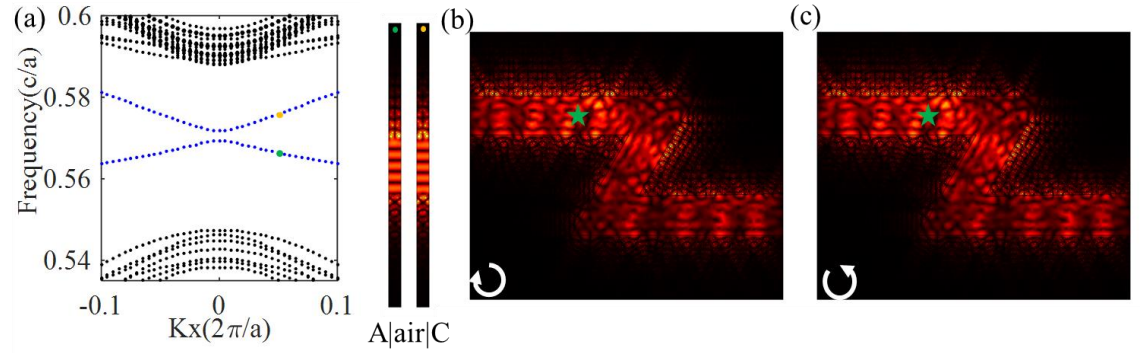

Figure S6 | Projected band structure of $A|air|C$ and its waveguide states. a Projected band structure of $A|air|C$ (left), whereas right two panels denote mode profiles ($|E_z|$) of the non-topological waveguide modes at different eigenfrequencies marked by the green and yellow dots. **b, c** Excited non-topological waveguide states in a Z-shaped waveguide channel for different polarized chiral sources.

Supplementary Note 7: Chirality (or directionality) map in domain B for $A|B_5|C$

From the Ez phase distributions of the helical waveguide modes, as presented in right panels of Fig.1b in the main text, we show that the large-area helical waveguide modes have inherent pseudospin-chirality locking property. The local chirality (or directionality)[5] of the helical waveguide modes could be characterized by the Stokes parameters, which for the waveguide mode labeled by the red dot in Fig.S7a in domain B is given in Fig.S7b, from which one can see that the chirality (i.e., the direction of propagation) of these large-area helical waveguide modes depends on the location of the chiral source. The excited wave propagations of the large-area waveguide state with source at a,b,c are shown in Fig.S7c-e, from which one can clearly see that the propagation direction of the topological waveguide states can be solely controlled by the location of the chiral source.

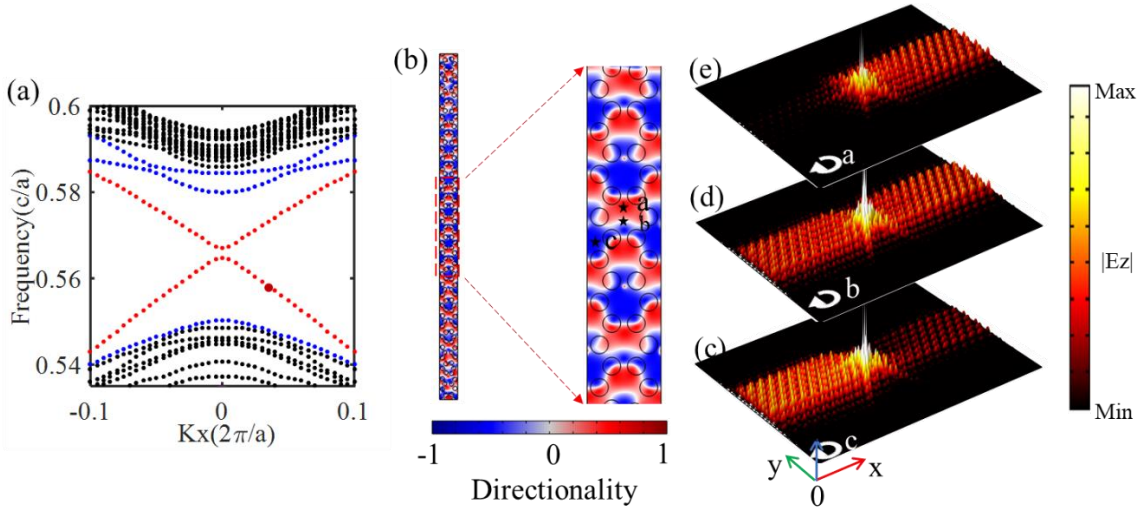

Figure S7 | Topological properties of the large-area helical waveguide modes in $A|B_5|C$ **. a** Projected band structure of $A|B_5|C$. **b** Chirality (or directionality) map in domain B for mode labeled by the red dot. **c-e** Excitation of the helical waveguide mode using the same chiral source but at different locations labeled by black stars a, b, and c.

Supplementary Note 8: Schematic of disorder and cavity defects used in the simulations and experiments for $A|B_5|C$

Figure S8a shows the simulated propagation of the topological waveguide modes in $A|B_5|C$ against a disordered region in domain B, from which one can see that the propagation of the topological waveguide mode can pass through the disordered region without being backscattered, compared to the case without disorder. These simulation results have been successfully confirmed in experiments, where the disordered region in domain B is constructed by moving the lattice unit cells marked within the rectangle to the left, up and right away from their normal location by $0.04a$ (see Fig.S8b-c). Figure S8d shows the simulated propagation of the topological waveguide modes in $A|B_5|C$ against an air cavity in domain B, from which one can see that though the existence of the air cavity along the propagation path, the topological waveguide modes can pass through it without being backscattered. The shape of the air cavity introduced in the simulations and experiments is shown in Fig.S8e-f.

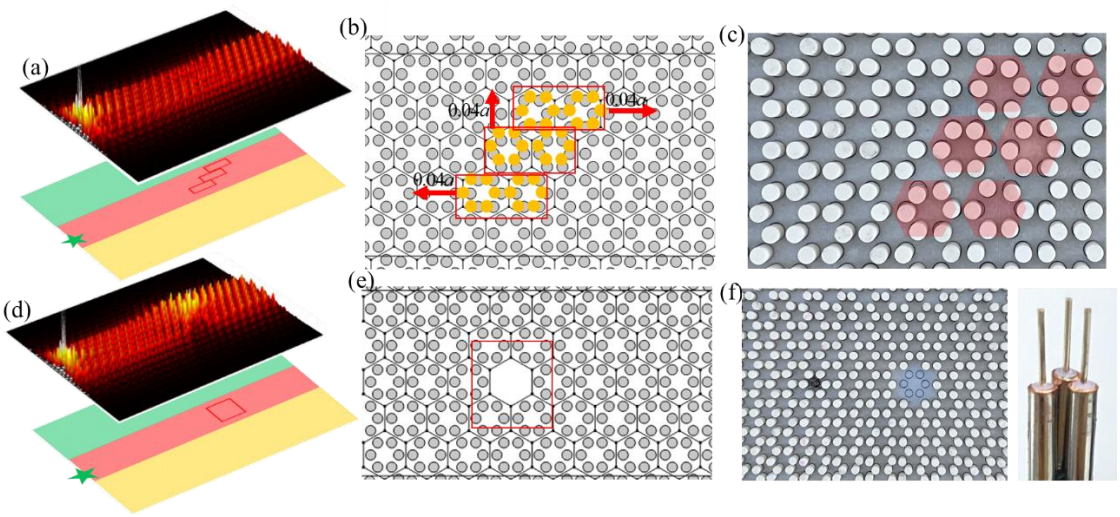

Figure S8 | Illustration of the disorder and defects used in the simulations and experiments for $A|B_5|C$ **. a** Simulated wave propagation for the topological waveguide modes in $A|B_5|C$ with disorder; bottom panel denotes the geometrical structure of the $A|B_5|C$ heterostructure with disorder. **b, c** Distributions of disorder in the simulations and experiments, respectively. **d** Simulated wave propagation in $A|B_5|C$ with an air cavity; bottom panel denotes the geometrical structure of the $A|B_5|C$ heterostructure with the air cavity. **e, f** Position of the air cavity in the simulations and experiments, respectively; right panel denotes the chiral source, which is composed by three antennas in the experiments.

Supplementary Note 9: Large air cavity that breaks the unidirectional propagation of topological waveguide modes.

In the main text, we show that the topological waveguide modes can tolerate much large defects due to their large mode width. However, one can expect that when the transverse size of the defect is comparable to the mode width, the topological property of unidirectional propagation will be broken. To demonstrate this, we study two large air defects shown in Fig.S9. From the results, one can see that the propagation of the unidirectionally launched wave is backscattered strongly, indicating the breakdown of the topological protection. Hence there exists a critical size of the air-cavity, below which the topological properties of the topological waveguide modes can persist. Figure S9b shows that the unidirectionally launched wave is more strongly scattered by C10, which indicates that the topological properties of the topological waveguide modes against such an air cavity are completely broken. It is worth noting that the large-area property of the waveguide modes is not destroyed. This is because bulk states in domain B with the double Dirac-cone dispersion are confined by two boundaries of the domain B.

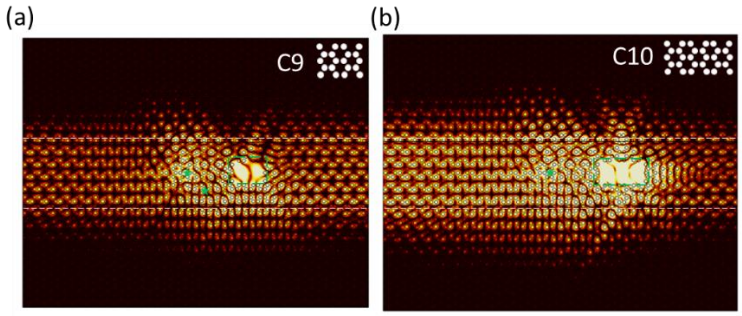

Figure S9 | Simulated propagations of the topological waveguide modes in $A|B_5|C$ **with two air cavities. A**-C9 and **b**-C10**.**

Supplementary Note 10: Poynting vector maps in domain B with air-cavities

Figure S10a shows the Poynting vector map for a unidirectionally launched wave in $A|B_5|C$ without any imperfections, from which one can see that the energy flows unidirectionally in domain B to the right. Figure S10b-d show the Poynting vector distributions in domain B with unidirectional propagations of the topological waveguide modes in a straight waveguide channel with air cavity defects. Figure S10e shows the Poynting vector distributions in a waveguide channel where the wave is completely backscattered by the air cavity, which indicates that topological properties of the topological waveguide modes are destroyed. Figure S10f-i show the Poynting vector distributions in cases where the unidirectionally launched wave can bypass the air cavity defects and the results also show that increasing the transverse size of the air cavity has a more significantly effect on the wave propagation than increasing the longitudinal size of the air cavity.

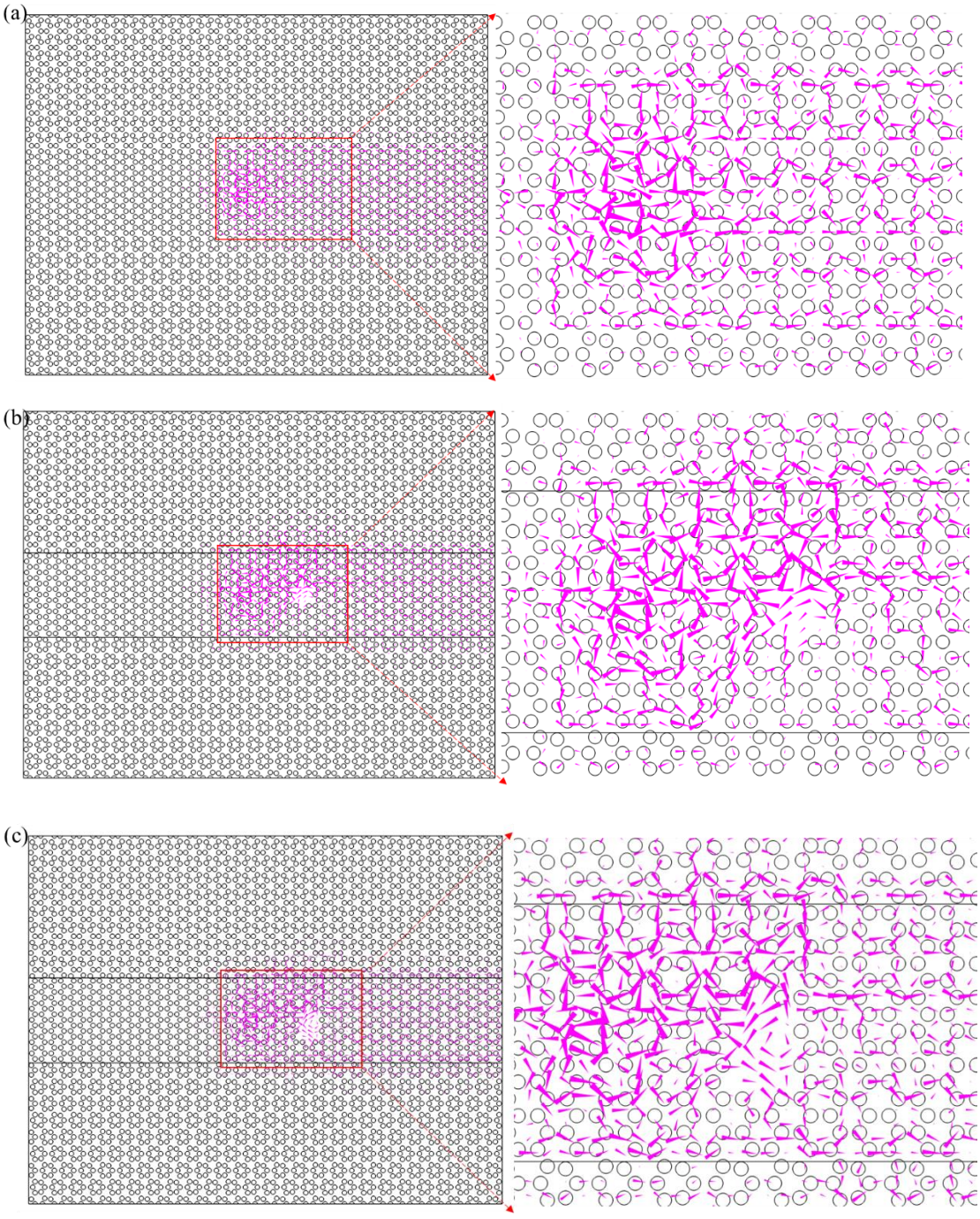

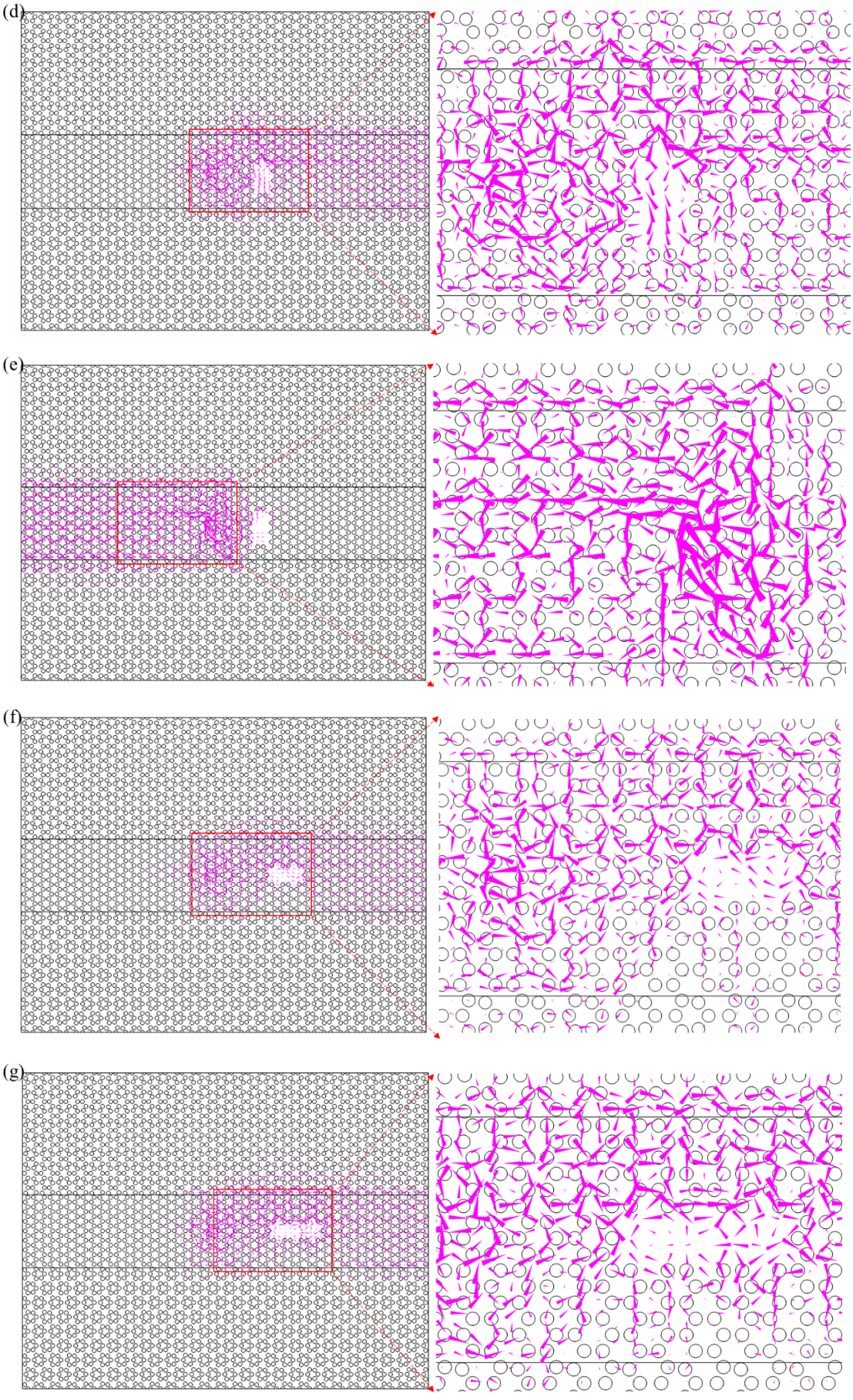
(d)
(e)
(f)
(g)

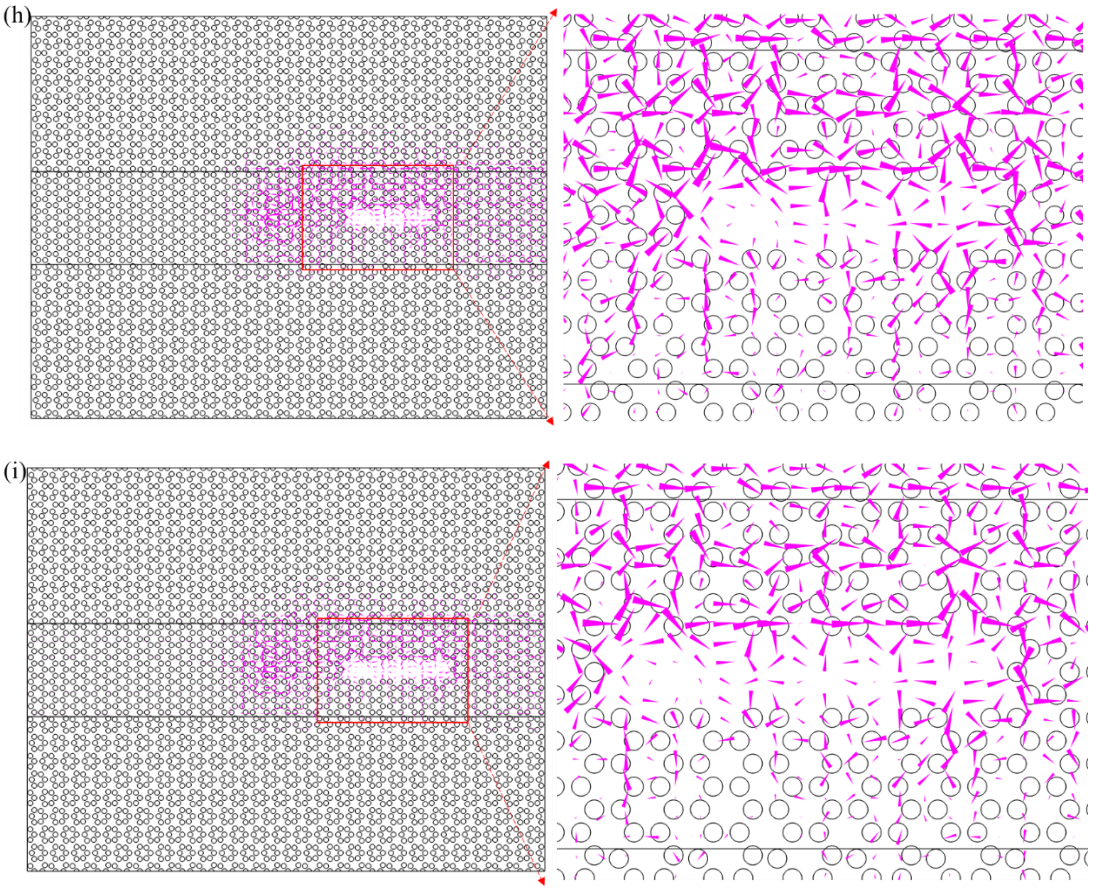

Figure S10 | Poynting vector distributions of LPWSs against different air-cavities in domain B. a-i Poynting vector of LPWSs in $A|B_5|C$ for different air-cavities, where pink arrows denote Poynting power flows, right panels are enlarged views marked as red rectangles.

Supplementary Note 11: Applications of large-area topological waveguide modes

Apart from the topological channel intersection and topological energy concentrator presented in the main text, additional applications of the large-area topological waveguide mode, such as topological energy splitter and topological cavity with tunable mode confinement are demonstrated in Figs.S11(c-f).

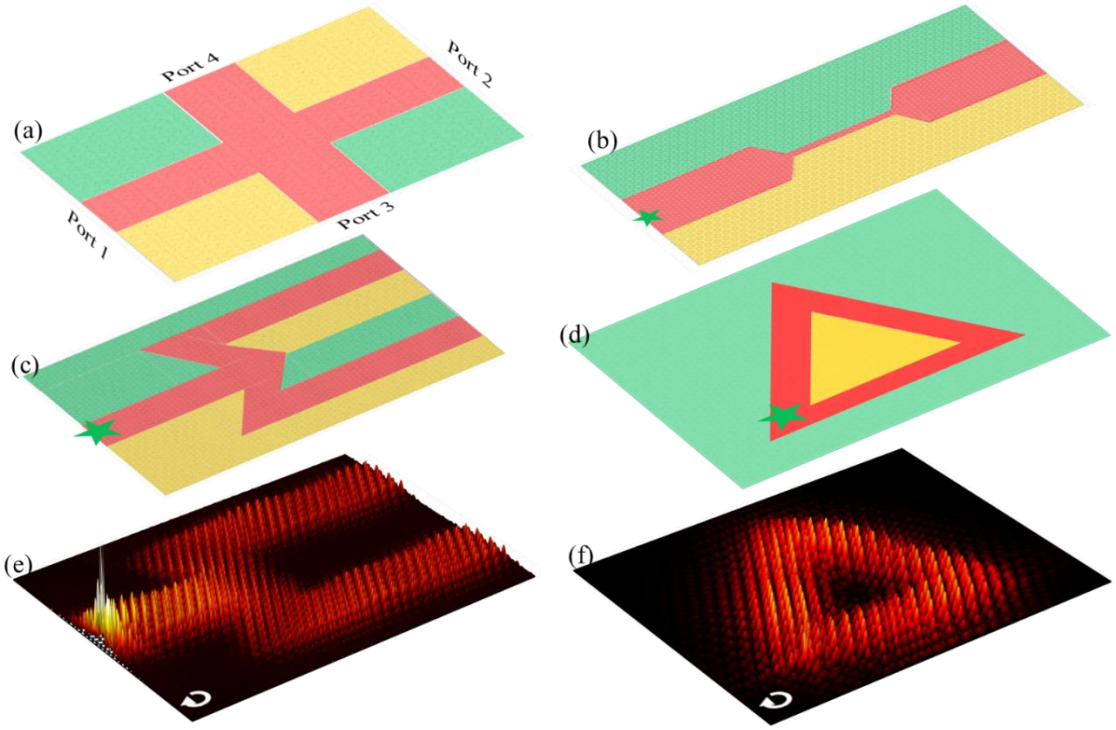

Figure S11 | Applications of large-area topological waveguide modes. a Schematic of a topological channel intersection. **b** Schematic of a topological energy concentrator. **c, e** Schematic and simulated result of a topological energy splitter. **d, f** Schematic and simulated result of a topological cavity with tunable mode confinement.

References

1. Wu, L. H. & Hu, X. Scheme for achieving a topological photonic crystal by using dielectric material. Phys. Rev. Lett. 114, 223901 (2015).
2. Wu, L. H. & Hu, X. Topological properties of electrons in honeycomb lattice with detuned hopping energy. Sci. Rep.6, 24347 (2016).
3. Kariyado, T. & Hu, X. Topological states characterized by mirror winding numbers in graphene with bond modulation. Sci. Rep. 7, 16515 (2017).
4. Wang, X. X. & Hu, X. Reconfigurable topological waveguide based on honeycomb lattice of dielectric cuboids. Nanophotonics 9, 3451–3458 (2020).
5. Lan, Z. H. et.al. Second-harmonic generation via double topological valley-Hall kink modes in all-dielectric photonic crystals. Phys. Rev. A 103, L041502 (2021).